JACS
JOURNAL OF THE AMERICAN CHEMICAL SOCIETY
pubs.acs.org/JACS
Article

Single-Atom High-Temperature Catalysis on a Rh_1O_5 Cluster for Production of Syngas from Methane

Yu Tang,[¶] Victor Fung,[¶] Xiaoyan Zhang,[¶] Yuting Li,[¶] Luan Nguyen, Tomohiro Sakata, Kotaro Higashi, De-en Jiang,* and Franklin Feng Tao*

Cite This: J. Am. Chem. Soc. 2021, 143, 16566−16579
Read Online

ACCESS | Metrics & More | Article Recommendations | Supporting Information

ABSTRACT: Single-atom catalysts are a relatively new type of catalyst active for numerous reactions but mainly for chemical transformations performed at low or intermediate temperatures. Here we report that singly dispersed Rh_1O_5 clusters on TiO_2 can catalyze the partial oxidation of methane (POM) at high temperatures with a selectivity of 97% for producing syngas (CO + H_2) and high activity with a long catalytic durability at 650 °C. The long durability results from the substitution of a Ti atom of the TiO_2 surface lattice by Rh_1, which forms a singly dispersed Rh_1 atom coordinating with five oxygen atoms (Rh_1O_5) and an undercoordinated environment but with nearly saturated bonding with oxygen atoms. Computational studies show the back-donation of electrons from the d_{z^2} orbital of the singly dispersed Rh_1 atom to the unoccupied orbital of adsorbed CH_n ($n > 1$) results in the charge depletion of the Rh_1 atom and a strong binding of CH_n to Rh_1. This strong binding decreases the barrier for activating C−H, thus leading to high activity of Rh_1/TiO_2. A cationic Rh_1 single atom anchored on TiO_2 exhibits a weak binding to atomic carbon, in contrast to the strong binding of the metallic Rh surface to atomic carbon. The weak binding of atomic carbon to Rh_1 atoms and the spatial isolation of Rh_1 on TiO_2 prevent atomic carbon from coupling on Rh_1/TiO_2 to form carbon layers, making Rh_1/TiO_2 resistant to carbon deposition than supported metal catalysts for POM. The highly active, selective, and durable high-temperature single-atom catalysis performed at 650 °C demonstrates an avenue of application of single-atom catalysis to chemical transformations at high temperatures.

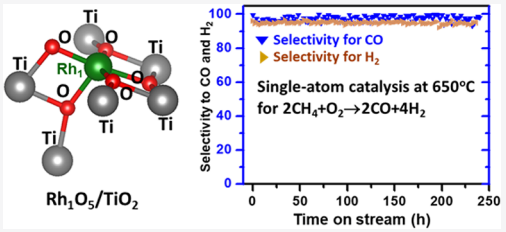

INTRODUCTION

The production of synthesis gas (syngas) from methane has mainly been achieved through the catalytic steam reforming of methane (SRM) at 800 °C or through noncatalytic homogeneous partial oxidation of methane (POM) at >1127 °C.[1−4] Steam reforming of methane at >800 °C has been the predominant catalytic process in the industrial production of syngas since the 1930s.[2−5] Supported Ni catalysts have been the main industrial catalysts for the steam reforming of methane, which suffers from a serious issue of carbon deposition despite the fact that a significant number of catalysts of SRM were reported in the literature.[2−4] Although the addition of more H_2O to the reactor is used to suppress coke formation in methane reforming, it unfortunately creates new problems in terms of increasing the H_2/CO ratio through the water−gas shift reaction. A high H_2/CO ratio consequently limits the direct use of the CO and H_2 mixture in downstream processes, mainly Fischer−Tropsch synthesis.[2−4] Meanwhile, the noncatalytic POM is a homogeneous reaction processed at an extremely high temperature (>1127 °C), which consumes a significant amount of energy to maintain the reaction temperatures and thus results in a large carbon footprint and a need for the costly maintenance of the reactors.

The limitations of catalytic SRM and noncatalytic POM drove explorations into catalytic POM as early as the 1920s.[2−4] Compared to noncatalytic POM performed at >1127 °C, catalytic POM can be performed at reaction temperatures lower than 1127 °C, significantly reducing energy costs. Due to the mildly exothermic nature of POM at room temperature, performing POM at the lower temperatures is thermodynamically feasible as long as its kinetics can be promoted by a catalyst. Significant efforts in this area were made in the last few decades as reviewed in the literature.[2,3,6−8] Ni supported on alumina was the main catalyst for POM studied in the 1920s−1940s.[9,10] In the 1980s−1990s, Ni catalysts modified with different supports including Y_2O_3, Co_3O_4, ZrO_2, UO_2, ThO_2, and rare earth oxides were then reported.[2−4] The main problem of these Ni-based POM catalysts is the formation of whisker carbon, which clogs reactors substantially.[11−17] In addition, by using $CaAl_2O_4$, $AlPO_4$-5, alkaline metal oxide-modified alumina, or $Ca_{0.8}Sr_{0.2}TiO_3$ as a support of Ni, the thermal stability of Ni-based catalysts was improved to some extent, although the selectivity for producing CO and H_2 was

Received: June 21, 2021
Published: September 30, 2021

Downloaded via GEORGIA INST OF TECHNOLOGY on September 14, 2022 at 18:51:03 (UTC).
See https://pubs.acs.org/sharingguidelines for options on how to legitimately share published articles.

© 2021 American Chemical Society

https://doi.org/10.1021/jacs.1c06432
J. Am. Chem. Soc. 2021, 143, 16566−16579

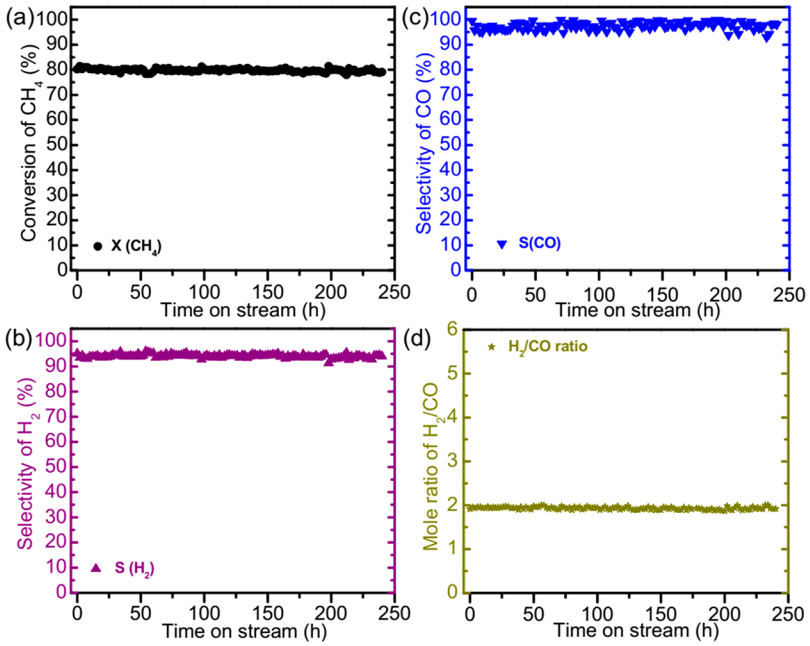

Figure 1. Catalytic durability of the Rh_1/TiO_2 catalyst (0.037 wt % Rh/TiO_2) for POM in a period of 10 days. (a) Conversion of CH_4 at 650 °C; (b) selectivity for producing H_2 at 650 °C; (c) selectivity for producing CO at 650 °C; (d) H_2/CO molar ratio at 650 °C. Catalysis conditions: catalyst is 50 mg of 0.037 wt % Rh/TiO_2; the gas fed to the reactor is a mixture of 25 mL/min of 10% CH_4 and 25 mL/min of 5% O_2; catalysis temperature is 650 °C.

sacrificed.[18−22] Unfortunately, the issue of deactivation of nickel catalysts by carbon deposition during POM remains unresolved so far.[2]

In the 1980s, Green et al. reported $Ln_2M_2O_7$ (Ln = La, Pr, Eu, La, Dy, Yb, Ba, Bi, and M = Ru, Ir, Pt, Rh) catalysts exhibiting high activity and selectivity, which led to a renaissance in catalytic POM studies.[4,10,23,24] Their early reports on $Ln_2M_2O_7$ inspired a large number of studies on precious metals and related catalysts since the 1980s;[2] Pt, Pd, and Rh, with a loading of 0.5−5.0 wt % on different types of supports including alumina foam and mixed oxides were investigated for POM. Through these studies, an ordering of activity impacted by a support was suggested: Y_2O_3 > La_2O_3 > MgO > Al_2O_3 > SiO_2 and Y_2O_3 > ZrO_2 > TiO_2.[25] These supported noble metals are highly active for POM, although their thermal stabilities were not reported in detail.[2] Different from these Ni-based and noble metal-based catalysts, molybdenum carbide was reported by York et al.[26−28] This type of catalysts has an activity similar to noble metals; however, it readily deactivates through a two-step process under reaction conditions, where molybdenum carbide is first oxidized to molybdenum oxide and then vaporization occurs at high temperatures under 1 atm of pressure.[2,3,6,7,26−28] Despite these significant efforts in the development of different types of POM catalysts, these reported catalysts have still suffered from either carbon deposition and/or a loss or a harmful restructuring of the active catalyst components during POM.

The literature has demonstrated that single-atom catalysts of many transition metals including Pt, Pd, and Rh exhibit distinctly different catalytic performances for a number of reactions at the relatively low temperature.[29−39] Compared to the continuously packed metal atoms on the surface of a metal particle, a singly dispersed metal atom, or an isolated metal atom, anchored on the surface of a nonmetallic support, typically an oxide, is in a distinctly different chemical and coordination environment and thus exhibits a very different electronic state. For instance, Rh atoms were anchored to the internal surface of the micropores of the aluminosilicate ZSM-5 through proton exchange, making the single-atom catalysts, Rh_1@ZSM-5; these reported single-atom sites immobilized in the 0.56 nm wide micropores of ZSM-5 are active for the synthesis of acetic acid and methanol through coupling of CH_4, CO, and O_2 in the microporous reactor, where reactant molecules are delivered through the diffusion of dissolved gas molecules in aqueous solution under a high-pressure gas phase at low temperatures of ≤150 °C.[40,41] These singly dispersed metal atoms, or single atoms, on a nonmetallic surface are typically undercoordinated, and either electronically deficient or rich, which offers them a high tendency to bind to a reactant molecule or intermediate. However, one major challenge of single-atom catalysts is their short durability at high catalysis temperature and low reusability as their singly dispersed single-atom sites readily sinter at elevated temperatures.[42,3,43,44] Thus, most single-atom catalysts function well at room temperature or a relatively low temperatures (≤300 °C) but not at high temperatures (≥450 °C), although a significant portion of chemical productions of chemical and petrochemical industries are performed at high temperatures driven by thermodynamics or/and kinetics. Notably, the high temperature defined here is different from that of high-temperature processes in industries, which run at 800 °C or higher.

Herein we report a high-temperature single-atom catalyst, Rh_1/TiO_2, which is highly active for POM at 650 °C. During the high temperature catalysis at 650 °C, its Rh_1 atom coordinates with five O atoms, a nearly saturated coordination shell. This single-atom catalyst exhibits long durability and extraordinary catalytic performance at 650 °C for about 240 h and high reusability from 20 repeat runs in the temperature range of 450−650 °C.

https://doi.org/10.1021/jacs.1c06432
J. Am. Chem. Soc. 2021, 143, 16566−16579

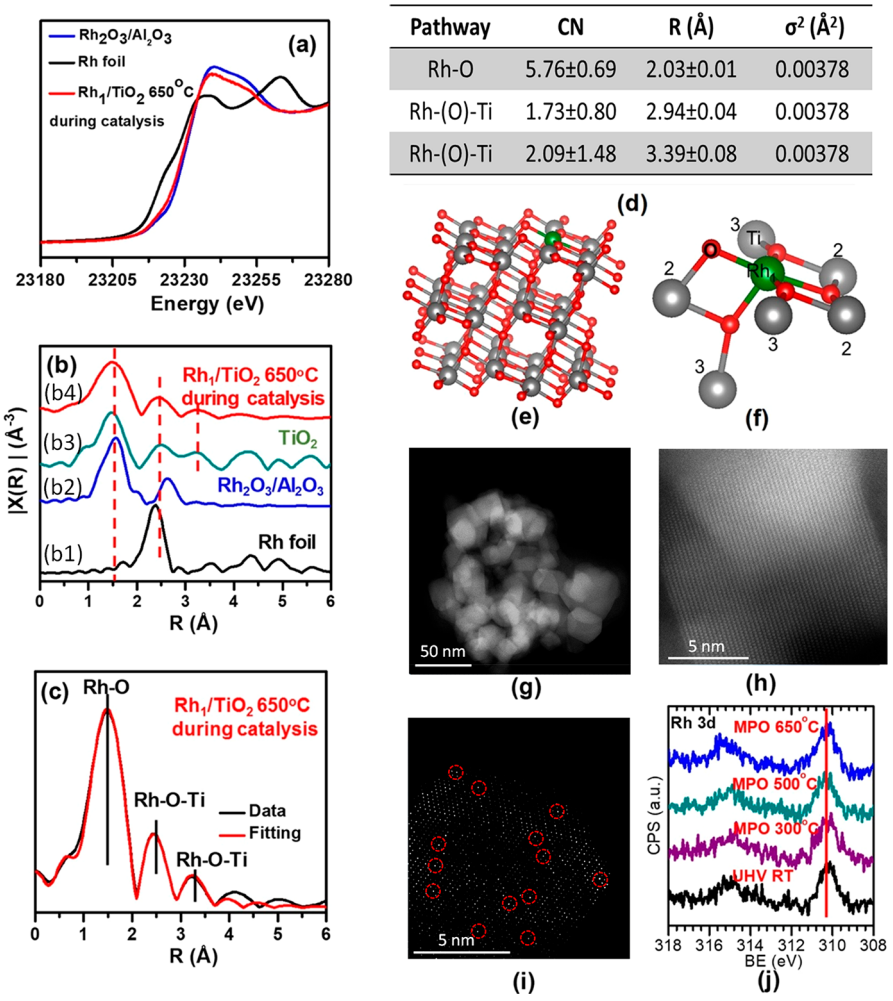

Pathway	CN	R (Å)	σ^2 (Å^2)
Rh-O	5.76±0.69	2.03±0.01	0.00378
Rh-(O)-Ti	1.73±0.80	2.94±0.04	0.00378
Rh-(O)-Ti	2.09±1.48	3.39±0.08	0.00378

Figure 2. In situ and operando studies of the 0.037 wt % Rh/TiO_2(Rh_1/TiO_2) catalyst for POM. (a–c) In-situ XANES and EXAFS studies of the Rh K-edge. (a) XANES data of Rh foil, Rh_2O_3/Al_2O_3, and Rh_1/TiO_2 under catalytic conditions of 650 °C; (b) k^2-weighted Rh K-edge EXAFS data in r space of (b1) Rh foil collected in air, (b2) Rh_2O_3/Al_2O_3 collected in air, and (b4) Rh_1/TiO_2 collected in the flowing mixture of CH_4 and O_2 through an in situ study approach of EXAFS, and (b3) k^2-weighted Ti K-edge EXAFS data in r space of TiO_2 collected in air; (c) k^2-weighted Rh K-edge EXAFS data in r space of Rh_1/TiO_2 collected in the flowing mixture of CH_4 and O_2 through an in situ study approach of EXAFS (black line) and the fitted curve (red line). (d) List of fitting parameters including bond lengths and coordination number. (e) Optimized structural model of catalyst Rh_1/TiO_2. (f) Coordination environment of Rh_1 atoms in the optimized structural model of (e). (g) Large-scale TEM image of catalyst particles after catalysis at 650 °C for 240 h. (h) High-resolution TEM image of a particle of (g); (i) High-resolution aberration-corrected HAADF-STEM images visualizing singly dispersed Rh atoms anchored on TiO_2 marked in red circles. (j) AP-XPS spectra of Rh 3d of Rh_1/TiO_2 in UHV at 25 °C, in the mixture of 0.8 Torr CH_4 and 0.4 Torr O_2 at 300 °C, 500 °C, and 650 °C; MPO as known as POM stands for partial oxidation of methane.

RESULTS AND DISCUSSION

Catalytic Performance of Single-Atom Catalyst Rh_1/TiO_2. The single-atom catalyst Rh_1/TiO_2 was prepared through a deposition precipitation method modified for the preparation of Rh_1/TiO_2.[45−47] Rh(III) cations were introduced to the surface of TiO_2 nanoparticles followed by drying at 60 °C in air overnight and then annealing at 650 °C in air for 4 h. Based on ICP-AES measurements, the actual loading of Rh on TiO_2 is 0.037 wt %. Details of the preparation can be found in the Experimental Methods and Computational Approaches section. For convenience, 0.037 wt % Rh/TiO_2, Rh_1/TiO_2, and Rh_1O_5/TiO_2 are interchangeably used to refer to the same catalyst in this article, depending on which piece of specific information (concentration, single dispersion, or coordination) of this single-atom catalyst is emphasized. The chemical and coordination environment of the singly dispersed Rh_1 atoms will be discussed in the next section.

Compared to the inactive TiO_2 nanoparticles for POM in the temperature range of 300−700 °C (Figure S1a), the Rh_1/TiO_2 catalyst is highly active for POM in the range of 450−650 °C under a flow of a mixture of 25 mL/min 10% CH_4 and 25 mL/min 5% O_2 (Figure S2). At 650 °C, 50 mg of 0.037 wt % Rh/TiO_2 has a conversion of 80% for CH_4 (Figure 1a). The selectivities for producing H_2 and CO at 650 °C are 96% and 98%, respectively (Figure 1b and c). This catalytic activity and selectivity on Rh_1/TiO_2 remain after over 240 h of time on stream (Figure 1). There was no interphase diffusion limit since the conversion of CH_4 remained nearly the same, while the flow rate of the mixture of CH_4 and O_2 varied in the range of 30−100 mL/min (Figure S3). The observed byproducts are mainly CO_2 and H_2O, which are formed from a competing reaction channel, the complete oxidation of methane; here the selectivities for forming byproducts CO_2 and H_2O are 4% and 2%, respectively. In the kinetics-controlled regime, the $Rh_1/$

https://doi.org/10.1021/jacs.1c06432
J. Am. Chem. Soc. 2021, 143, 16566−16579

TiO_2 catalyst exhibits an extraordinarily high turnover rate of 2300 H_2 molecules produced from a Rh_1-based site per minute at 650 °C. Details of calculation of the turnover rate (TOR) can be found in Section 7.2 of the Supporting Information (SI). The distinct difference in catalytic activity between pure TiO_2 (Figure S1) and Rh_1/TiO_2 (Figure 1) clearly shows the crucial role of the anchored Rh_1 atom, although the loading is only 0.037 wt %. To test the reusability of the catalyst, catalysis was performed from 300 to 650 °C on Rh_1/TiO_2, followed by cooling to 300 °C before the next cycle for a total of 20 cycles on Rh_1/TiO_2. Compared to the catalytic performance of the first cycle (Figure S2a), the decay in catalytic activity and selectivities at the 20th cycle (Figure S2b) is less than 4% over a period of 20 cycles. This suggests quite a high reusability for Rh_1/TiO_2.

The single-atom catalyst Rh_1/TiO_2 also exhibited quite a long durability for POM at 650 °C for at least 240 h. As shown in Figure 1a, the conversion of CH_4 (80%) remained without any decay at the 240th hour compared to the zeroth hour. In addition, the selectivity for the production of H_2 and CO remained at 96% and 98%, respectively, under 650 °C for the whole duration with negligible changes (Figure 1b and c). The molar ratio of produced H_2/CO remained at 2.0 during the catalysis at 650 °C for 240 h (Figure 1d). The preservation of catalytic activity, selectivities, and H_2/CO molar ratio in Figure 1 confirms the high durability of the Rh_1/TiO_2 catalyst at the high temperature of 650 °C, suggesting that the chemical and coordination environments of Rh atoms of this catalyst remained unchanged (Figure 1), which is further supported by in situ and operando characterizations of 0.037% Rh/TiO_2 under the catalytic conditions described below.

Chemical and Coordination Environment of Rh Atoms in Single-Atom Catalyst Rh_1/TiO_2. The chemical and coordination environments of Rh atoms of 0.037 wt % Rh/TiO_2 at the atomic scale were investigated through in situ XANES and EXAFS studies. A 20 mg amount of 0.037 wt % Rh/TiO_2 (catalyst #1) was loaded into the XAS reactor (XANES and EXAFS); a mixture of 10 mL/min 10% CH_4 and 10 mL/min 5% O_2 was introduced; thus, the gas hourly space velocity (GHSV) in the XAS reactor of in situ XAS studies at the beamline end-station was the same as that of catalytic measurements performed at our catalysis lab. The catalyst was heated to 650 °C in the flow of the aforementioned reactant mixture. High activities and selectivity of the catalyst during the in situ XAS studies at 650 °C were confirmed through an online mass spectrometer analyzing the composition of gas received through a glass capillary installed on the outlet of the XAS reactor. During the in situ studies, the generated fluorescence due to absorption of the Rh K-edge was collected when the catalyst was in a mixture of 10% CH_4 and 5% O_2 after catalysis at 650 °C for 4 h. The Rh K-edge of Rh_1/TiO_2 (catalyst #1) at 23231.0 eV (red line in Figure 2a) is close to that of Rh_2O_3 nanoparticles supported on Al_2O_3 (blue line in Figure 2a),[48] suggesting that Rh atoms of 0.037% Rh/TiO_2 are in an oxidized state. In addition, the observed energy spectrum of the Rh K-edge of Rh_1/TiO_2 (red line in Figure 2a) is quite consistent with the energy spectrum of the Rh K-edge (red line in Figure 3) theoretically simulated by using the structural model of a single-atom catalyst (Figure 2e) optimized in the computational studies. The proposed structural model of 0.037% Rh/TiO_2 (Figure 2e) will be described and discussed in detail later in this article.

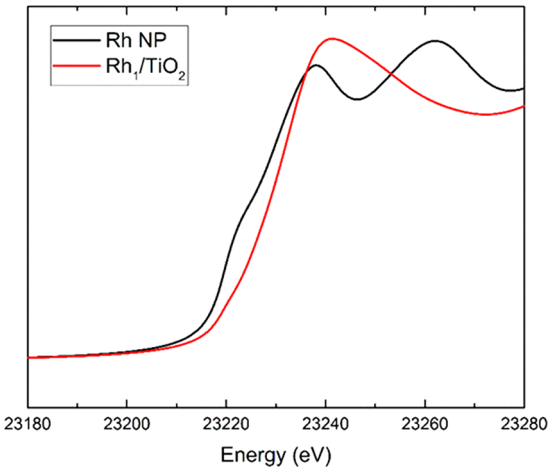

Figure 3. Theoretically simulated Rh K-edge energy spectra of the Rh K-edge of single-atom catalyst Rh_1/TiO_2 and Rh nanoparticles. The red curve is the simulated spectrum of Rh_1 anchored on TiO_2 through the structural mode optimized with DFT (Figure 2e and f); black curve is the simulated spectrum of Rh nanoparticles consisting of 79 atoms (Rh_{79}) optimized with DFT (Figure S24b). The simulated spectra of Rh_1/TiO_2 and Rh nanoparticles are shown to be consistent with the observed spectra of Rh_1/TiO_2 (red curve in Figure 2a) and Rh foil (black curve in Figure 2a).

In the Fourier transformed *r*-space spectra of the Rh K-edge of 0.037% Rh/TiO_2 (Figure 2b4), a main peak at 1.50 Å was observed and readily assigned to Rh−O bonds, consistent with Rh−O bonds of the reference sample, Rh_2O_3 nanoparticles supported on Al_2O_3 (Figure 2b2), and those reported in references.[48−50] Here 1.50 Å is the Rh−O distance in the *r*-space spectrum before a phase correction. We note all the distances of EXAFS studies described in the following paragraphs are distances before phase correction except for a specific note. Compared to the observed Rh−O−Rh peak at 2.63 Å from the reference sample (Rh_2O_3/Al_2O_3 in Figure 2b2), no such a Rh−O−Rh peak was observed in the spectra of 0.037 wt % Rh/TiO_2 (Figure 2b4). In addition, the spectrum of Rh_1/TiO_2 (Figure 2b4) does not have the peak of Rh−Rh bonds of Rh foil observed at 2.35 Å (Figure 2b1). Thus, neither the peak of the Rh−O−Rh bond of Rh_2O_3 nanoparticles (2.63 Å) nor the peak of the Rh−Rh bond of metal Rh nanoparticles (2.30 Å) was observed in the *r*-space spectrum of 0.037 wt % Rh/TiO_2 (Figure 2b4). The difference in coordination environment among Rh_1/TiO_2, Rh_2O_3/Al_2O_3, and Rh foil was supported by wavelet transform (WT) of EXAFS data of references samples (Rh foil and Rh_2O_3/Al_2O_3) and the catalyst, 0.037 wt % Rh/TiO_2 (Figure 4). In Figure 4a, there is one major contour maximum observed in the WT plot of Rh foil at (11.6 $Å^{-1}$, 2.30 Å), which is attributed to the first-shell Rh−Rh coordination pathway in the foil sample. In the WT plot of the Rh_2O_3 reference sample (Figure 4b), there is one major contour maximum at (7.7 $Å^{-1}$, 1.5 Å) for the first-shell Rh−O coordination pathway and another three minor contour bands at k = 7.68, 10.5, and 13.4 $Å^{-1}$, which are assigned to the coordination with surrounding O and Rh atoms at R = 2.5−2.6 Å in the second shell (Rh−O−Rh). However, in the WT plot of the Rh_1/TiO_2 catalyst under POM at 650 °C (Figure 4c), only one maximum at (7.6 $Å^{-1}$, 1.5 Å) is found for the Rh−O coordination pathway, suggesting the lack of the second-shell Rh−O−Rh on Rh_1/TiO_2. In addition, the contour maxima of Rh−Rh coordination which had been

https://doi.org/10.1021/jacs.1c06432
J. Am. Chem. Soc. 2021, 143, 16566−16579

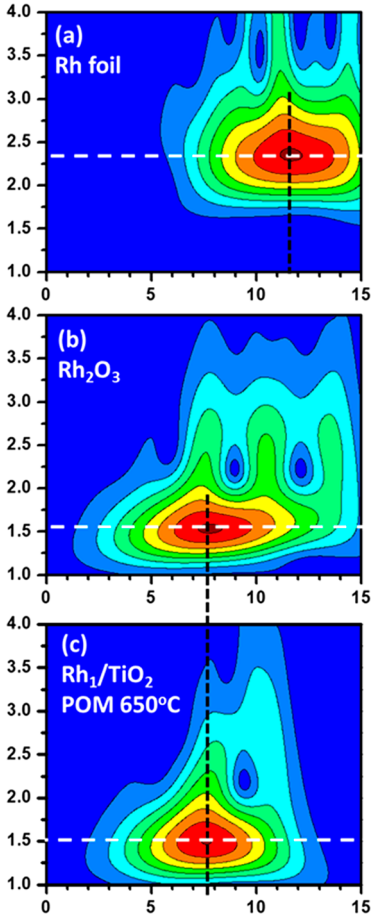

Figure 4. Wavelet transformation of EXAFS data of reference samples Rh foil (a), Rh_2O_3/Al_2O_3 nanoparticles (b), and the catalyst 0.037 wt % $Rh/TiO_2(Rh_1/TiO_2)$ (c). Wavelet transformation parameters: HAMA Fortran package, *k* weight 2, Morlet function, kappa = 5, and sigma = 1.

found in Rh foil and Rh_2O_3/Al_2O_3 are not observed in the WT plot of Rh_1/TiO_2, suggesting the lack of Rh−Rh coordination in the catalyst during POM. Figure 4 suggests that Rh atoms are singly dispersed in 0.037 wt % Rh/TiO_2 instead of forming Rh metal NPs or Rh_2O_3 NPs, further evidenced in the Diffuse Reflectance Infrared Fourier Transform Spectroscopy (DRIFTS), CO chemisorption measurements, and AP-XPS studies and to be discussed in the following paragraphs.

It could be argued that the peak of Rh−O−Ti of Rh_1/TiO_2 at 2.50 Å in Figure 2b4 could not be fully distinguished from the peak of Rh−Rh of Rh foil at 2.30 Å in Figure 2b1 due to the limited resolution of these *r*-space spectra. The following characterizations allow us to deduce that no Rh−Rh bond contributed to this peak of Rh−O−Ti of Rh_1/TiO_2 at 2.50 Å in Figure 2b4. First, compared to the vibrational feature of CO adsorbed on Rh nanoparticles at 1872 and 2060 cm^{-1} in the spectra of diffuse reflectance infrared Fourier transform spectroscopy (DRIFTS) (Figure S7), the lack of the two peaks in the DRIFTS spectrum of the used Rh_1/TiO_2 (Figure 5) suggests that no Rh nanoparticles formed on the surface of 0.037 wt % Rh/TiO_2 during catalysis at 650 °C since 1872 and 2060 cm^{-1} are attributed to stretching of CO molecules adsorbed on the surface of Rh metal nanoparticles (Figure S10) or the Rh single crystal.[51] The detailed pretreatment and collection of data of DRIFT spectra were described in Section

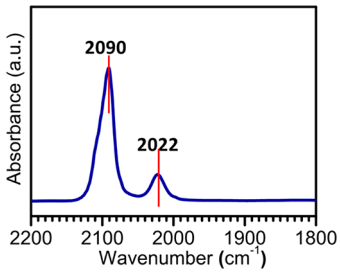

Figure 5. DRIFT study of CO adsorbed on 0.037 wt % Rh/TiO_2 (Rh_1/TiO_2).

5 in the SI. Peaks at 2090 and 2022 cm^{-1} in the DRIFTS spectrum of Rh_1/TiO_2 in Figure 5 are assigned to asymmetric and symmetric stretching of C≡O of two CO molecules bound to a single Rh atom; this binding configuration is called a geminal-dicarbonyl binding configuration in which two CO molecules are simultaneously bound to a metal atom. The vibrational signature in Figure 5 is very similar to that of single-atom catalysts reported in the literature.[32−37] For Rh nanoparticles, such a geminal-dicarbonyl binding configuration should be quite minor or even not present since Rh atoms on the surface of a Rh nanoparticle are continuously packed. Thus, DRIFT studies suggest that no Rh NPs were formed on TiO_2 of 0.037 wt % Rh/TiO_2 during catalysis at 650 °C. Second, the measurement of the dispersion of Rh atoms of 0.037% Rh/TiO_2 by CO chemisorption showed that >97.5% of Rh atoms of the used 0.037% Rh/TiO_2 are singly dispersed on TiO_2; this further suggests that the fraction of Rh atoms of 0.037% Rh/TiO_2 catalyst that could potentially form Rh nanoparticles is lower than 2.5%. The single dispersion of Rh atoms on the surface of the 0.037% Rh/TiO_2 catalyst is suggested from CO chemisorption measurement, the vibrational signature of CO chemisorbed on 0.037 wt % Rh/TiO_2, and in situ EXAFS studies. It is further supported with the lack of Rh nanoparticles on the used catalyst (Figure 2g and h) and the observation of singly dispersed Rh atoms (Figure 2i).

The peak at 2.50 Å in *r*-space of the Rh K-edge of 0.037 wt % Rh/TiO_2 (Figure 2b4 or Figure 2c) was fitted to Rh−O−Ti. Figure 2c presents the fitted *r*-space spectrum (in red), which matches the experimental spectrum (in black) very well. The fitting parameters are listed in Figure 2d. This fitting shows (1) O and Ti atoms are in the first and second shells of the Rh_1 atom of 0.037 wt % Rh/TiO_2 under the catalytic conditions at 650 °C, respectively, (2) the coordination number of oxygen atoms in the closest shell of the Rh_1 atom is about 5.76 ± 0.69, and (3) the coordination number of Ti atoms in the second shell to Rh_1 is about 3.82. The average coordination number of oxygen atoms bonded to a singly dispersed Rh_1 atom is 5.76 ± 0.69, suggesting that a Rh atom can substitute for either a Ti atom of the top layer (Figure S5a, Figure 2e or f) of TiO_2 or a Ti atom in the subsurface or deeper layer of TiO_2 since the coordination number of O to a Ti atom in the top layer of the Ti atom or in the subsurface of TiO_2 is 5 or 6, respectively. In fact, the vast majority of Rh atoms of the used 0.037 wt % Rh/TiO_2 substitute for Ti atoms of the top layer in terms of the surface of TiO_2 instead of Ti atoms in the subsurface of TiO_2 of Rh_1/TiO_2 since the dispersion of Rh atoms on the surface of the 0.037 wt % Rh/TiO_2 is 97.5% based on the CO chemisorption measurements (Section 2 in the SI).

As most users are usually only granted a beam time of 1−3 days, continuously tracking the catalyst structure with EXAFS

https://doi.org/10.1021/jacs.1c06432
J. Am. Chem. Soc. 2021, 143, 16566−16579

in a period of 10 days was not realistic. The following in situ XAS studies including XANES and EXAFS of catalyst #2 were performed. To be specific, catalyst #2 is 0.037 wt % Rh/TiO_2, which has already been used for POM at 650 °C at the catalysis lab before XAS studies. In situ XANES and EXAFS studies of catalyst #2 were performed under the same in situ conditions as catalyst #1. Fittings the *r*-space spectrum of Rh K-edge of catalyst #2 (Figure S8b) shows that Rh atoms of catalyst #2 were still singly dispersed. The fitting parameters of Figure S8b of catalyst #2 listed in Figure S9 suggest the number of oxygen atoms coordinated with the Rh_1 atom and bond length of Rh−O of catalyst #2 are similar to catalyst #1 (Figure 2d). The high similarity between the *r*-space spectra of catalyst #1 and catalyst #2 suggests the preservation of the coordination environment of Rh_1 atoms of Rh_1/TiO_2 during catalysis at 650 °C. This structural preservation upon catalysis at 650 °C well rationalizes the long durability of Rh_1/TiO_2 in terms of catalytic performance at 650 °C (Figure 1).

The replacement of Ti cations in the surface lattice of TiO_2 by Rh cations was supported by the observation of periodic peaks at 2.63 and 3.35 Å of the Rh K-edge in the *r*-space spectrum as marked with red dashed lines in Figure 2b4. These periodic peaks are in good agreement with the periodic peaks in the *r*-space spectrum of the Ti K-edge of TiO_2 (Figure 2b3 and Figure S11a). Based on the literature,[52,53] the appearance of the two peaks of the Ti K-edge at 2.54 and 3.30 Å in Figure S11a was contributed from the periodic arrangement of Ti atoms (Ti−O−Ti^{α} and Ti−O−Ti^{β}) in the crystal lattice of pure TiO_2 (Figure 6). Compared to the *r*-space spectrum of the Ti K-edge of Ti atoms of TiO_2 (Figure 2b3), a very similar periodic pattern in the *r*-space spectrum of the Rh K-edge of Rh atoms of Rh_1/TiO_2 (Figure 2b4) was observed. This similarity suggests that these Rh_1 atoms substituted for Ti atoms in the surface lattice of TiO_2 (Figure S10f).

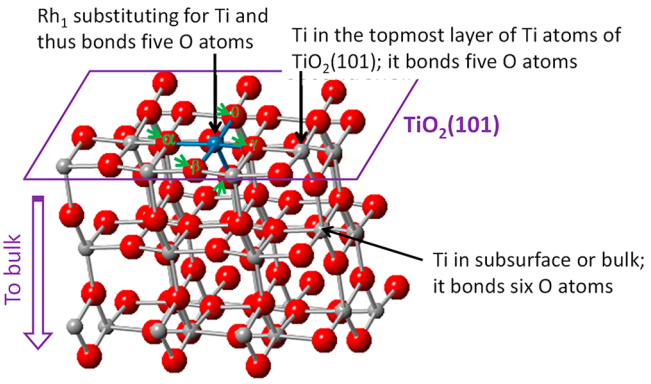

Figure 6. Structure of Rh_1/TiO_2 in which Rh_1 substituted for a Ti atom in the surface lattice of $TiO_2(101)$, optimized with DFT. Rh, O, and Ti atoms are shown in blue, red, and gray, respectively. The five O atoms (directly bonding to Rh_1 on the $TiO_2(101)$ surface are marked with five green arrows. Compared to the first coordination shell of a Ti atom in the subsurface or bulk, the first coordination shell of the Rh_1 is nearly saturated, and thus it exhibits high stability. On the other hand, the unsaturation of the first coordination shell of the Rh_1 makes the Rh_1 reasonably strongly bound to C atoms of CH_4, CH_3, and CH_2 and thus makes Rh_1 highly active in the transformation of CH_4 to CH_3, CH_3 to CH_2, and CH_2 to CH. The nearly saturated environment of Rh_1 makes the singly dispersed Rh_1 atom thermodynamically stable; thus, the Rh_1/TiO_2 exhibits a long duration at 650 °C for 240 h without decay of the catalytic performance and high reusability.

The chemical state of Rh atoms of Rh_1/TiO_2 during POM at 650 °C was tracked with ambient-pressure X-ray photoelectron spectroscopy (AP-XPS).[54] The formation of CO and H_2 on Rh_1/TiO_2 during AP-XPS studies was confirmed with an online mass spectrometer installed on the AP-XPS device, showing that the catalyst was active during the AP-XPS characterization at 650 °C. The high binding energy of Rh $3d_{5/2}$ of Rh_1/TiO_2 at 310.2 eV (Figure 2j) suggests that Rh_1 atoms are in a cationic state during catalysis at 650 °C. The high binding energy of the Rh 3d peak of Rh_1/TiO_2 during catalysis observed experimentally is consistent with the electron transfer from d_{z^2} of the Rh_1 atom to CH_4 proposed through computational studies.

As (101) is the dominant surface of this catalyst Rh_1/TiO_2 based on HAADF-STEM studies (Figures S13b−d), $TiO_2(101)$ was chosen as the surface to anchor the Rh_1 atom in the theoretical simulations of the surface structure of Rh_1/TiO_2. Based on the surface structure of $TiO_2(101)$, the Rh atom could be anchored through a substitution mode (Figure S5a) or three capping-on modes (Figure S5b−d). Computations of the energies of the four optimized structural modes in Figure S5 show that the substitution mode of Rh_1/TiO_2 is most thermodynamically favorable. In this mode, a Rh atom substitutes for a Ti atom in the top layer of Ti atoms of the (101) surface of TiO_2, and thus each Rh_1 atom bonds with five oxygen atoms as shown in Figure 6, Figure 2e, or Figure S6a. The five O atoms bonding to Rh_1 on the $TiO_2(101)$ surface are marked with five green arrows in Figure 6. Here, Rh_1O_5 is used to refer to the coordination environment of a Rh_1 atom of the catalyst during catalysis. The reasonableness of the thermodynamically favorable substitution mode is supported by the consistency between the bond parameters of Rh−O obtained from the structural optimization in computational studies and these parameters generated from EXAFS experiments. Thus, the substitution structural mode in Figure 6 was used as the surface structure in the simulation of the catalytic mechanism of POM on the single-atom catalyst, Rh_1/TiO_2.

To shed light on the POM mechanism, the adsorption and transformation of CH_4 on Rh_1/TiO_2 were explored through computational studies. Based on the literature,[55−58] chemisorption of CH_4 typically involves the formation of an alkane σ complex. Charge transfer and orbital coupling between CH_4 and Rh_1 were studied with DFT. Figure 7a is the top view of the optimized Rh_1/TiO_2 with a chemisorbed CH_4 molecule through binding a C atom of CH_4 to the Rh_1 atom. The calculated electron-density-difference plots of CH_4 on Rh atom of Rh_1/TiO_2 are shown in Figure 7b; electron density of Rh_1 of Rh_1/TiO_2 transferring to the C atom of CH_4 is mapped based on the color bar. Meanwhile, in the case of bare TiO_2, electron density of Ti of TiO_2 hardly transfers to CH_4 (Figure 7c). This specific difference can be found in the calculated Bader charges (Figure S13). The substantial charge transfer from Rh_1 of Rh_1/TiO_2 to the C atom of CH_4 is supported by the elongation of C−H from 1.096 Å of the free CH_4 molecule to 1.115 Å of the chemisorbed CH_4 molecules on the Rh_1 atom; however, the C−H bond distance of CH_4 adsorbed on bare TiO_2 (Figure S14) is 1.099 Å, which is nearly the same as the free molecule.

To further understand the significance of Rh_1 in orbital coupling between CH_4 and Rh_1, partial density of states (PDOS) of CH_4 and the Rh atom of Rh_1/TiO_2 with

https://doi.org/10.1021/jacs.1c06432
J. Am. Chem. Soc. 2021, 143, 16566−16579

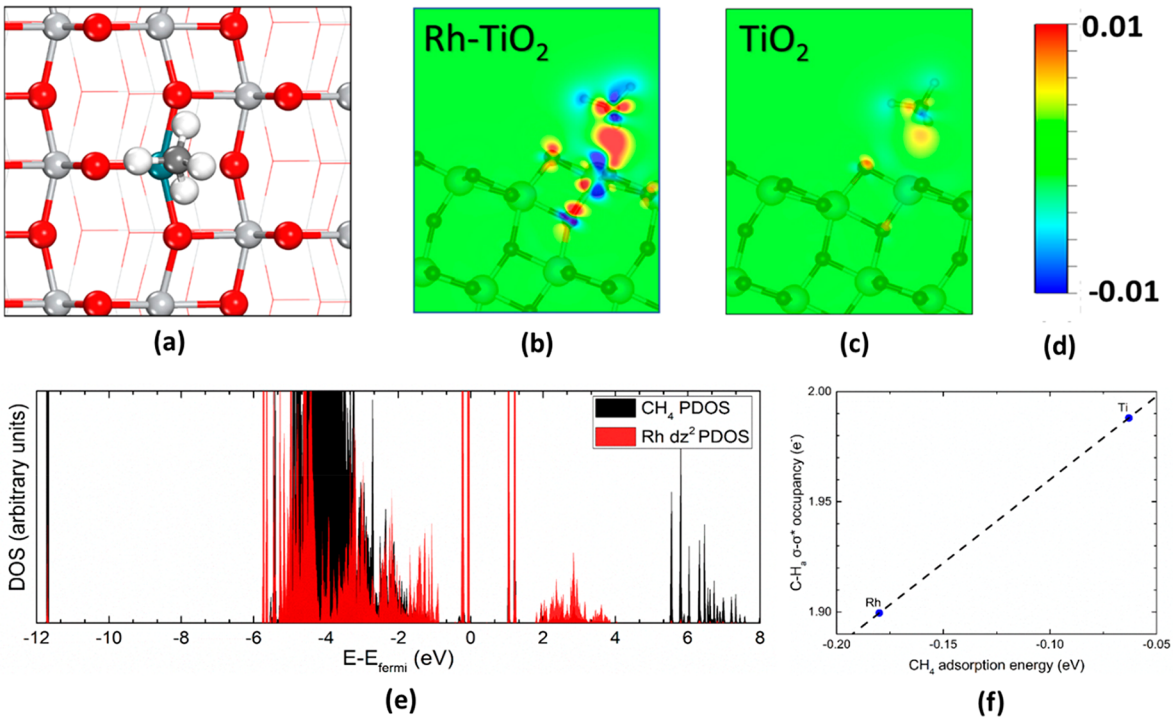

Figure 7. Geometrical and electron configurations and orbital coupling of CH_4 adsorbed on TiO_2(101) from DFT calculations. (a) Top view of Rh_1/TiO_2 with chemisorbed CH_4. (b and c) Electron-density-difference plots of CH_4 on the Rh atom of Rh_1/TiO_2 and CH_4 on the Ti atom of bare TiO_2. (d) Color bar used to show relative electron density in (b) and (c); warmer color stands for higher electron density. (e) Partial density of states (PDOS) plots of the adsorbed CH_4 on Rh_1/TiO_2 obtained from DFT calculations; the projected states on d_{z^2} are shown for the Rh site. (f) Correlation between the C−H_a σ−σ* occupancy and methane adsorption strength from periodic natural bond orbital (NBO) analysis.

chemisorbed CH_4 were calculated. As shown in Figure 7e, molecular orbitals of CH_4 (black lines) mix most strongly with the d_{z^2} orbital of the substituting Rh_1 atom (red lines) since electron density of the d_{z^2} orbital of Rh_1 can back-donate to the unoccupied orbital of the adsorbed CH_4 molecule. This back-donation is consistent with the electron-density-difference plot in Figure 7b, which shows a significant charge depletion around the Rh_1 atom and the corresponding charge enhancement around CH_4. The electron-density difference can be evaluated through the color code of Figure 7d. Moreover, the natural bond orbital (NBO) analysis in Figure 7f shows a lower C−H σ−σ* occupancy on Rh_1/TiO_2 than that on bare TiO_2, suggesting that Rh_1 of Rh_1/TiO_2 is quite favorable for activating the C−H bond via back-donation to σ*. Thus, both electron density calculation and simulation of orbital coupling of CH_4 and Rh_1 show that Rh_1 is favorable for binding CH_4 and activating the C−H bond.

Molecular-Level Understanding of POM on Rh_1/TiO_2 at High Temperature. Extensive computational studies for optimizing intermediates and searching for transition states of POM were performed on the optimized structure of Rh_1O_5/TiO_2 shown in Figure 6. These theoretical simulations proposed a complete catalytic cycle consisting of 26 elementary steps starting from chemisorption of reactants to form two CO and four H_2 molecules on Rh_1/TiO_2 ($2CH_4 + O_2 \rightarrow 2CO + 4H_2$). A complete energy profile of intermediates and transition states of the entire pathway was plotted in panel 1 of Figure 8. All intermediates are listed in Figure S15 and Figure S16. Figure S17 and S18 present the structures of transition states of this complete reaction pathway of POM on Rh_1/TiO_2.

We first discuss O_2 activation. Notably, the activation of molecular O_2 on Rh_1/TiO_2 is distinctly different from that on an oxygen vacancy of a transition metal oxide. The activation was not performed at the beginning of the cycle, as the surface at the beginning does not present oxygen vacancies and the adsorption of molecular O_2 on the surface without oxygen vacancies is weak. Even if molecular O_2 is dissociated, the formed O atoms can thermodynamically favorably return to the gas phase. Step **t** to **u** in Figure S16 is the activation of reactant O_2 through insertion of molecular O_2 between the Rh_1 atom and its nearest Ti atom in the intermediate **t**. Notably, this insertion step is kinetically barrierless and thermodynamically exothermic (panel 1 in Figure 8), suggesting a different path for activating molecular O_2 on Rh_1/TiO_2 in contrast to dissociation of O═O on the oxygen vacancy on the transition metal oxides. Different from the barrierless kinetics of molecular O_2 on this single-atom catalyst, Rh_1/TiO_2, the kinetic barrier for activation of O_2 on Co_3O_4,[59] TiO_2,[60] and CeO_2[61] is in the range of about 0.5−2.0 eV, which varies at different faces and vacancies. Compared to the activation of O_2 on an oxygen vacancy of transition metal oxides, this distinctly different barrierless activation mechanism of O_2 on the site of Rh_1/TiO_2 demonstrated the significance of Rh_1 in the high activity of Rh_1/TiO_2 for POM. The presence of both an undercoordinated Rh_1 atom and its nearby oxygen vacancies makes dissociative adsorption of molecular O_2 significantly downhill with little or no barriers, thus stabilizing the adsorbed O atoms even at high temperatures.

As can be seen from panel 2 of Figure 8, the Rh_1O_5 plays a crucial role in progressively activating CH_4 to form CH_3, CH_2, and CH before CH inserts into Rh_1-O^{θ} toward forming a CO molecule (see the inset in panel 1 of Figure 8 for the Greek

https://doi.org/10.1021/jacs.1c06432
J. Am. Chem. Soc. 2021, 143, 16566−16579

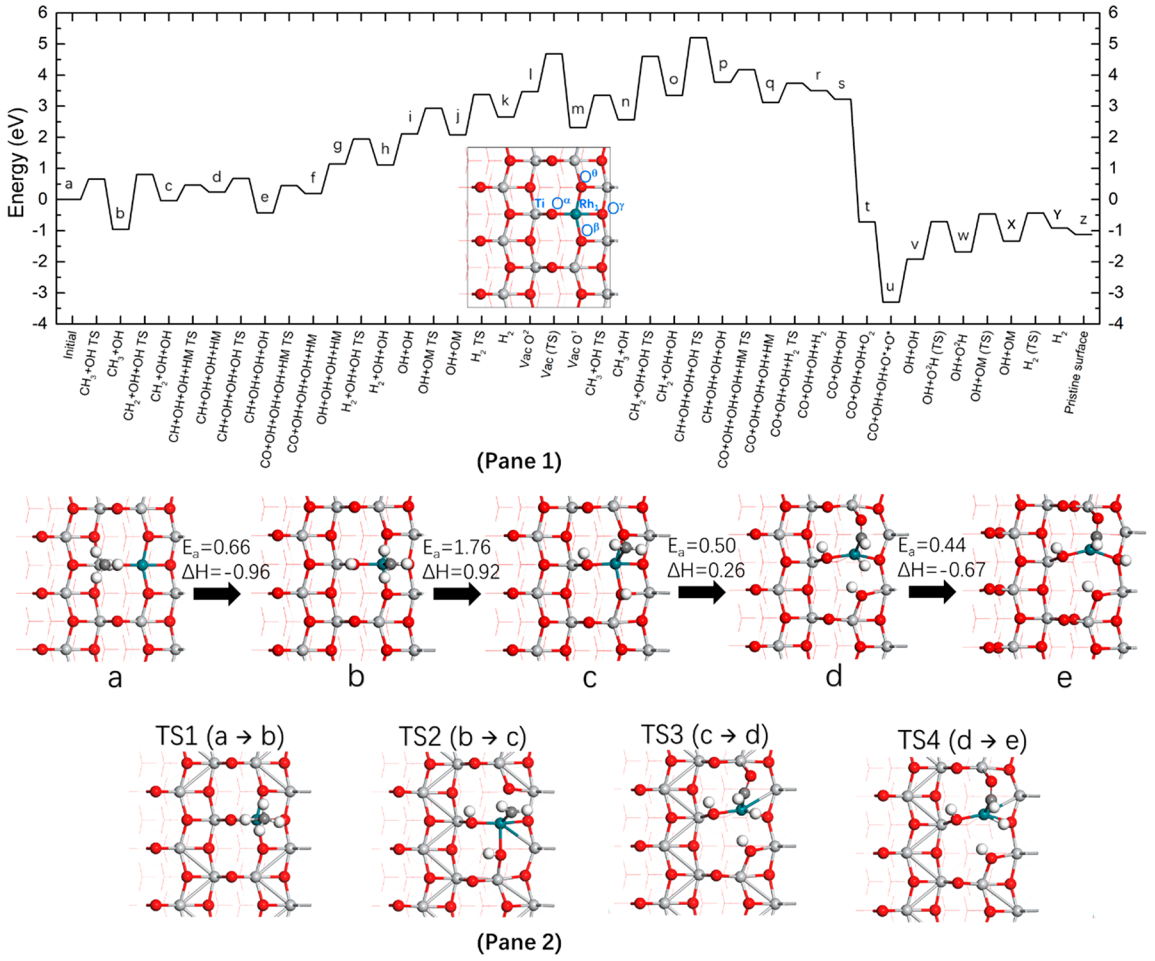

Figure 8. Energy profile of the complete pathway of POM consisting of 26 elementary steps on Rh_1/TiO_2 (panel 1) and optimized structures of intermediates (**a**, **b**, **c**, **d**, and **e**) of activation of CH_4 on Rh_1O_5 to form CH_3 (**a** → **b**), CH_2 (**b** → **c**), and CH (**c** → **d**) and the transition state 1 (**a** → **b**), transition state 2 (**b** → **c**), transition state 3 (**c** → **d**), and transition state 4 (**d** → **e**) (panel 2). Inset of panel 1 is the clean surface structure of Rh_1/TiO_2. All other intermediates and transition states are presented in Figures S15−S18.

labels given to O atoms around Rh_1). The coupling between C−H of CH_4 and Rh_1-O^{α} of Rh_1O_5 (**a** in panel 2 of Figure 8) breaks the first C−H bond, forming CH_3 on Rh_1 and H on O^{α} next to Rh_1 (**b** in panel 2 of Figure 8). C−H of CH_3 couples with Rh_1-O^{β}, forming CH_2 on Rh_1 and H on O^{β} next to Rh_1 (**c**). In terms of transformation of CH_2 to CH, Rh_1-O^{β} is broken and then CH is inserted into Rh_1-O^{θ} (**d**) and thus forms $Rh_1-C(H)-O^{\theta}-Ti$ (**e** in panel 2 in Figure 8). When −CH− is inserted, the H atom of CH transfers to Rh_1, forming $Rh_1-C-O^{\theta}-Ti$ (**f** in Figure S15). C−H activations on the Ti cation of bare $TiO_2(101)$ were simulated; as shown in panel 1 (black line) and panel 3 in Figure 9, each of the three transformations ($CH_4 \rightarrow CH_3$, $CH_3 \rightarrow CH_2$, $CH_2 \rightarrow CH$) on the Ti cation of bare $TiO_2(101)$ experiences a much higher activation energy than those on the Rh_1 cation of Rh_1/TiO_2. It clearly shows that Rh_1 on TiO_2 plays a significant role in activation of CH_4, which is consistent with the significant charge transfer from Rh_1 of Rh_1/TiO_2 to C of CH_4 (Figure 7b) but negligible charge transfer from Ti of bare TiO_2 to C of CH_4 (Figure 7c). After transformation of CH_4 to CH, whose C atom bonds with both O^{θ} and Rh_1, the C−H of CH breaks to lose its H atom to form a $-CO^{\theta}$ species whose C atom bridges on Rh_1 and Ti in **e**−**f** in Figure S15; then, both $Rh_1-C(=O^{\theta})$ and $(O^{\theta}=)C-Ti$ bonds break to form the first CO molecule in the step of **f**−**g**. Then, one O vacancy (O_{vac}) is created in **g** (Figure S15) due to the loss of O^{θ} as a part of the first product molecule CO. The coupling of two H atoms on Rh_1 forms the first H_2 molecule in **h**−**i** (Figure S15); so do the other two H atoms to form the second H_2 molecule in the step of **k**−**l** in Figure S15. Although the formation of H_2 is slightly uphill in terms of reaction enthalpy, the elevated temperatures under the reaction conditions make it favorable for H_2(g) to form rather than stay dissociatively adsorbed on the surface. Thus, the H atom adsorbed on the surface was a part of intermediate instead of part of the active site for POM.

The C−H of the second CH_4 molecule is activated on Rh_1 with a reasonably low activation barrier due to the relatively low coordination number of O atoms to Rh_1 in the intermediate **m** (**m**−**n** in Figure S16), forming CH_3 bound to Rh_1 in **n**; further C−H activation of CH_3 on Rh_1-O^{β} forms CH_2 whose C atom inserts between Rh_1 and O^{θ}, forming H_2C-O^{θ} and H_2C-Rh_1 in **o**; the formed CH_2 loses a H atom to form CH whose C atom bonds with both O^{θ} and Rh_1 in **p**; a CO-like species forms and its C atom bonds on Rh_1 after HC(=O) loses its H atom in **q**; coupling of two H atoms forms the third H_2 molecule in **r**; a molecular O_2 chemisorbs to bond with both Rh_1 and Ti in **t**; then, CO species adsorbed on Rh_1 desorb as the second CO molecule (**u**−**v** in Figure S16) in the catalytic cycle ($2CH_4 + O_2 \rightarrow 2CO + 4H_2$). Subsequently, the left two H atoms couple, forming the fourth H_2 molecule in

https://doi.org/10.1021/jacs.1c06432
J. Am. Chem. Soc. 2021, 143, 16566−16579

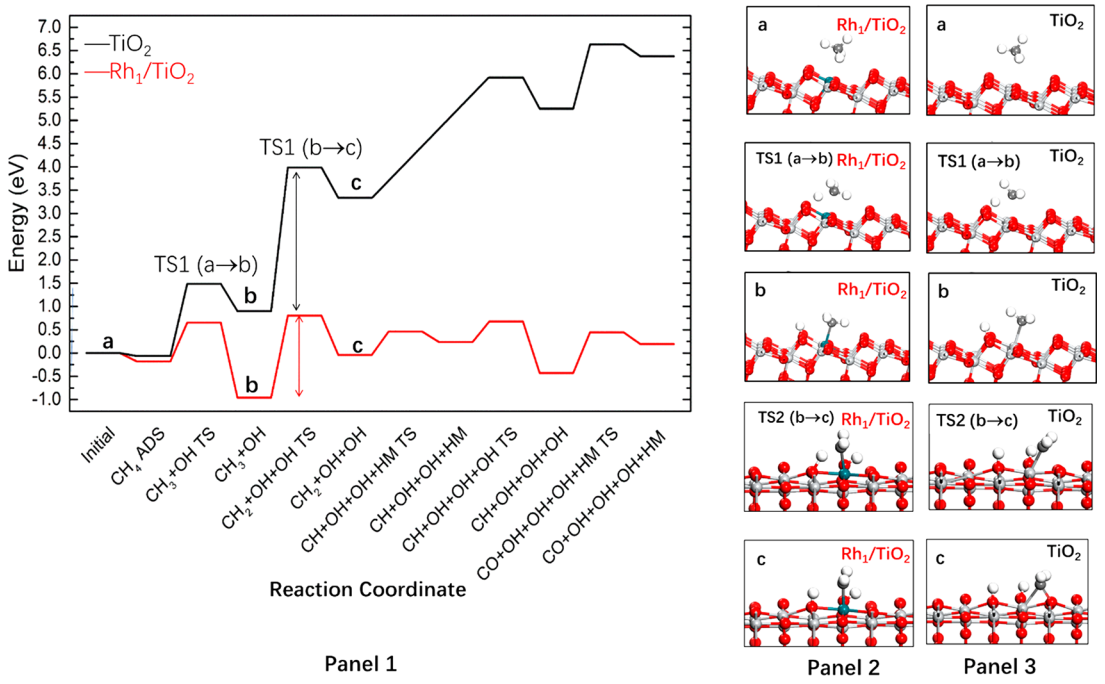

Figure 9. Energy profiles of transformations of CH_4 to CH_3, CH_3 to CH_2, and CH_2 to CH on Rh_1/TiO_2 and bare TiO_2. Obviously, the activation energies on the Ti cation of $TiO_2(101)$ is much higher than that of Rh_1/TiO_2. In addition, compared to the Ti atom on the surface of $TiO_2(101)$, the binding energies of CH_3 of intermediate **b** on Rh_1 is increased by 3.4 eV; thus, the energy of intermediate **b** on Rh_1/TiO_2 is much lower than that on TiO_2 (see the energy level of intermediate **b** in panel 1). The reasonably high binding energies of CH_3 to Rh_1 and the H atom to its neighboring O atom in intermediate **b** on Rh_1/TiO_2 results in a lower activation barrier for dissociating CH_3 to CH_2 and H to form intermediate **c** on Rh_1/TiO_2 than that on TiO_2, based on the Brønsted−Evans−Polanyi relationship.

v−**y**. The last H_2 in the catalytic cycle desorbs in **y**−**z**, regenerating the initial surface, where Rh_1 bonds with five O atoms (O^{α}, O^{β}, O^{γ}, O^{θ}, and one O in the subsurface). The regenerated surface (**z**) in Figure S16 is ready for the second catalytic cycle. Through the 26 elementary steps, two CH_4 and one O_2 participated in the catalytic reaction on the Rh_1O_5 site anchored on TiO_2, forming two CO and four H_2 molecules.

As shown in Figures S18 and S19, most intermediates of the POM on Rh_1/TiO_2 directly bind to Rh_1 and its adjacent O or nearest Ti atom, further confirming the crucial role of the Rh_1 on $TiO_2(101)$. Based on the energy profile of all intermediates and transition states in panel 1 in Figure 8, the three steps with the highest activation barriers are **b** → **c**, **n** → **o**, and **o** → **p**, with barriers of 1.76, 2.30, and 1.86 eV, respectively. **b** → **c** is the activation of C−H of CH_3 of the first CH_4 on Rh_1 to form CH_2; **n** → **o** is the activation of C−H of CH_3 of the second CH_4 on Rh_1 to form CH_2; **o** → **p** is the activation of CH_2 of the second CH_4 to form CH on Rh_1. Overall, the rate-determining step among the complete pathway of POM ($2CH_4 + O_2 \rightarrow 2CO + 4H_2$) on Rh_1/TiO_2 is the activation of C−H of CH_3 of the second CH_4 on Rh_1O_5 to form CH_2.

POM on Rh Nanoparticles Supported on TiO_2. In order to understand how the singly dispersed Rh_1 site could be different from its counterpart at high temperature, a surface consisting of closely packed Rh atoms was prepared for performing comparable studies on durability of the catalyst under the same condition as Rh_1/TiO_2. Such a surface can be found on Rh nanoparticles supported on TiO_2, termed Rh NP/TiO_2. The precursor of Rh NP/TiO_2 was prepared through impregnation, which is a method different from the deposition−precipitation method used in preparation of Rh_1/TiO_2. In the preparation of Rh NP/TiO_2, its precursor was reduced at 500 °C for 2 h and 650 °C for 2 h in 5% H_2 instead of calcination in air at 650 °C used in the preparation of Rh_1/TiO_2. Details of preparations of Rh NP/TiO_2 can be found in the Experimental Methods and Computational Approaches section. This Rh NP/TiO_2 catalyst is active for POM in the temperature range of 300−650 °C (Figure S19). Statistical counting of over 500 Rh NPs of the used catalyst Rh NP/TiO_2 shows that the average size of the Rh NPs supported on TiO_2 after catalysis at 650 °C for 240 h is approximately 3.0 nm (Figure S20). In the following sections, we use the labels Rh NP/TiO_2 and 6.3 wt %Rh/TiO_2 interchangeably, referring to the same catalyst. Compared to 50 mg of 0.037 wt % Rh/TiO_2 (Rh_1/TiO_2) at 450, 500, 550, or 650 °C (Figure S2), 50 mg of 6.3 wt % Rh/TiO_2 exhibits similar conversion of CH_4 at these corresponding temperatures, respectively. However, they exhibit quite different catalytic selectivities for producing H_2 or CO (Figure S2 versus Figure S19).

Notably, the similar conversion of CH_4 exhibited by the two catalysts (50 mg Rh NP/TiO_2 versus 50 mg Rh_1/TiO_2) at a temperature such as 650 °C does not suggest any similarity in activity of their catalytic site. As TiO_2 is completely inert for oxidation of CH_4 at 300−700 °C (Figure S1), the conversions of CH_4 of 50 mg of 6.3 wt % Rh/TiO_2 and 50 mg of 0.037 wt % Rh/TiO_2 depend on the numbers of Rh atoms exposed on the catalyst surface. For 50 mg of 0.037 wt % Rh/TiO_2, the amount of *the exposed Rh atoms on the surface* to catalyze the conversion of CH_4 is 1.75×10^{-7} mol; however, for 50 mg of 6.3 wt % Rh/TiO_2, the amount of *the exposed Rh atoms on the surface* to catalyze conversion of CH_4 is 1.07×10^{-5} mol. Calculations of the amounts of exposed Rh atoms on the catalyst surfaces are described in Section 6 of the SI. The ratio of the number of Rh atoms precipitated into the POM on 50 mg of 6.3 wt % Rh/TiO_2 to that on 50 mg of 0.037 wt % Rh/TiO_2 is about 61:1. Thus, although the conversions of CH_4 on

https://doi.org/10.1021/jacs.1c06432
J. Am. Chem. Soc. 2021, 143, 16566−16579

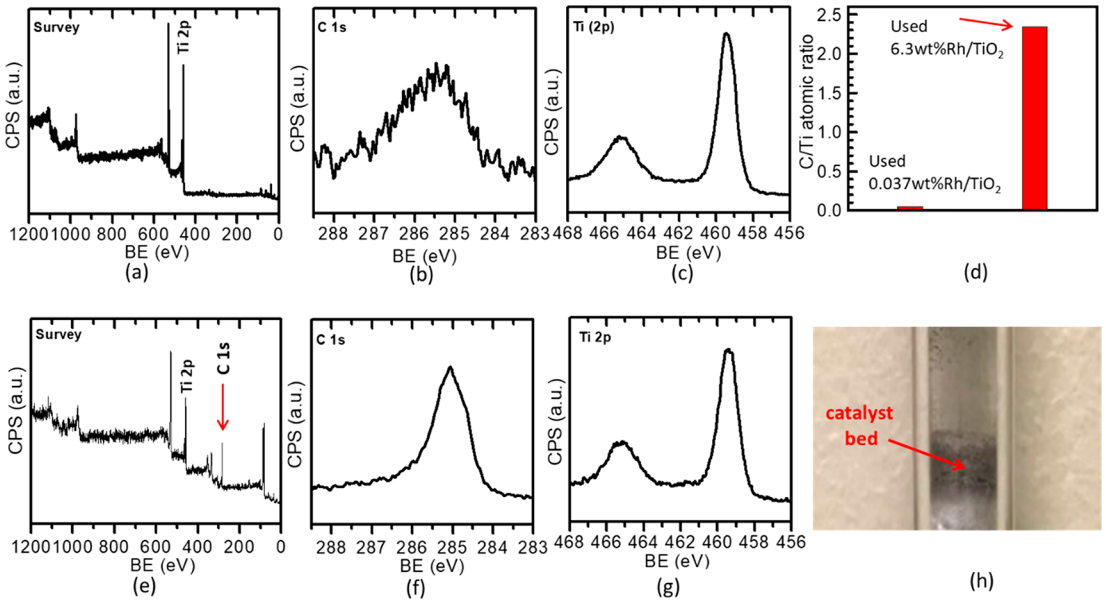

Figure 10. Formation of carbon layers on the Rh NP/TiO_2 catalyst but not on Rh_1/TiO_2 based on XPS studies of 0.037 wt % Rh/TiO_2 (Rh_1/TiO_2) and 6.3 wt % Rh/TiO_2 (Rh NP/TiO_2) after catalysis at 650 °C of 240 h. (a) Survey of the used 0.037 wt % Rh/TiO_2 (Rh_1/TiO_2) catalyst; (b) C 1s spectrum of the used 0.037 wt % Rh/TiO_2 (Rh_1/TiO_2) catalyst; (c) Ti 2p of the used 0.037 wt % Rh/TiO_2 (Rh_1/TiO_2) catalyst; (d) C/Ti atomic ratio of the used 0.037 wt % Rh/TiO_2 (Rh_1/TiO_2) catalyst and the used 6.3 wt % Rh/TiO_2 (Rh NP/TiO_2) catalyst; (e) survey of the used 6.3 wt % Rh/TiO_2 (Rh NP/TiO_2) catalyst; (f) C 1s spectrum of the used 6.3 wt % Rh/TiO_2 catalyst; (g) Ti 2p of the used 6.3 wt % Rh/TiO_2 catalyst; (h) photo of the used 6.3 wt % Rh/TiO_2 catalyst after catalysis at 650 °C for 240 h.

the two catalysts are seemingly similar, the activities of each exposed Rh atoms of the two catalysts are in fact *distinctly* different. The difference in catalytic activity between the two catalysts was further confirmed by measuring the turnover rates under the kinetics-controlled regime. As described in Section 4 of the SI, the reaction rate of each catalyst was measured when the conversion of CH_4 is less than 10%. With the measured reaction rate at 650 °C under a kinetics-controlled regime, the TORs of the two catalysts were calculated in Section 7 of the SI. The TOR of H_2 on a Rh atom of single-atom catalyst 0.037 wt % Rh/TiO_2 is 2300 H_2 molecules per minute, but it is only 35.0 H_2 molecules per minute on an exposed Rh atom of the Rh nanoparticle catalyst, 6.3 wt % Rh/TiO_2. Details of the calculations of TORs using data of kinetics studies are described in Sections 7.2 and 7.3 in the SI. Demonstrably, the activity in terms of TOR of the single-atom catalyst Rh_1/TiO_2 at 650 °C is much higher than the Rh nanoparticle catalyst, Rh NP/TiO_2, at the same temperature.

Durability of Single-Atom Catalyst Rh_1/TiO_2 at 650 °C. Other than the much higher activity of the Rh_1/TiO_2 catalyst at 650 °C than the Rh NP catalyst at this temperature, the high-temperature single-atom catalyst Rh_1/TiO_2 exhibits a much longer durability in catalytic performance than the Rh NP/TiO_2 (Figure 1 versus Figure S23). It is necessary to highlight that the comparison of the difference in durability of catalytic performance is for obtaining a fundamental understanding of the reason for the observed high-temperature durability of single-atom catalysts and not for developing a commercial POM catalyst for production of syngas in industries.

Compared to the nanoparticle catalyst (Rh NP/TiO_2), the single-atom catalyst (Rh_1/TiO_2) exhibits superior resistance to carbon formation. The continuously packed Rh atoms on the surface of Rh nanoparticles of Rh NP/TiO_2 (Figure S24b) cause CH_x (x = 0−2) species adsorbed on two adjacent Rh atoms to couple readily toward chain propagation, leading to the formation of a coke layer. As seen from XPS studies (Figure 10e, f, and g), thick carbon layers were formed on the used Rh NP/TiO_2 after POM at 650 °C for 240 h, while negligible amounts of carbon were formed on Rh_1/TiO_2 after 240 h of POM at 650 °C (Figure 10a, b, and c). The atomic ratio of carbon atoms of surface carbon layers to all titanium atoms in the surface region of used Rh NP/TiO_2 is about 2.5 (Figure 10d), suggesting the thickness of carbon is at least several atomic layers. It is much larger than that of Rh_1/TiO_2 used at 650 °C for 240 h. The experimentally observed facile formation of carbon layers on Rh NPs is supported by the quite high adsorption energy of atomic carbon on Rh atoms of the Rh nanoparticle surface uncovered in our computational studies (Figure S25b). Compared to the Rh atom on a Rh nanoparticle of 6.3 wt % Rh/TiO_2, the adsorption energy of atomic carbon on the singly dispersed Rh_1 atoms of 0.037 wt % Rh/TiO_2 is lower by 2.8 eV (Figure S25); this significant difference in adsorption energy of the carbon atom to Rh atoms of the two catalysts (Rh_1/TiO_2 versus Rh NP/TiO_2) results from the distinctly different coordination environment between Rh_1 of Rh_1/TiO_2 and Rh of Rh NP/TiO_2 (Figure S25). In terms of Rh_1/TiO_2, the singly dispersed Rh_1 atoms on TiO_2 do not provide opportunity for two CH_x (x = 0−2) species adsorbed on spatially isolated Rh_1 atoms to couple since CH_x species on Rh_1/TiO_2 are spatially separated. Thus, Rh_1/TiO_2 exhibits high resistance to formation of coke at 650 °C for a period of at least 240 h.

The high adsorption energy of atomic carbon on the surface of the metal Rh nanoparticle can rationalize the progressive decay of conversion of CH_4 to 60% at the 105th hour and to nearly only 20% at the 240th hour (Figure S23a). Along with the decay of catalytic activity, selectivities largely decreased to 86% for H_2 and 84% for CO at the 105th hour and to 42% for H_2 and 29% for CO at the 240th hour, respectively (Figure

https://doi.org/10.1021/jacs.1c06432
J. Am. Chem. Soc. 2021, 143, 16566−16579

S23b and c). This significant decay of catalytic activity of 6.3 wt % Rh/TiO_2 is consistent with the observation of a large amount of carbon formed on 6.3 wt % Rh/TiO_2 after catalysis for 240 h at 650 °C (Figure 10h).

The C/Ti atomic ratio of the 6.3 wt % Rh/TiO_2 catalyst used at 650 °C for 240 h is about 45 times that of the single-atom catalyst Rh_1/TiO_2 used at the same temperature for the same amount of time (Figure 10d), rationalizing the significant decay of the catalytic performance of 6.3 wt % Rh/TiO_2 results from the formation of carbon layers on Rh nanoparticles, which blocked the active sites. As reported in the literature,[2,4,11−17] there are two types of carbons formed on POM catalysts including encapsulated carbon, which blocks catalytic sites and thus obviously degrades catalytic performance, and whisker carbon, which forms on surface of a catalyst nanoparticle but sinks to one end of the catalyst nanoparticle and thus does not directly poison the catalyst surface but results in serious reactor clogging. As the reactor of the 6.3 wt % Rh/TiO_2 catalyst was not clogged after catalysis at 650 °C for 240 h, likely encapsulated carbon instead of whisker carbon was formed on Rh NPs of 6.3 wt % Rh/TiO_2. As these encapsulating carbon layers on the catalyst surface block the active sites, the catalytic activity clearly becomes degraded. The mechanism of deactivation of 6.3 wt % Rh/TiO_2 is interesting and worth further studies. As the theme of this article is the molecular-level understanding of the high-temperature single-atom catalytic chemistry of Rh_1/TiO_2 for POM, we leave the further studies of the deactivation of 6.3 wt % Rh/TiO_2 in POM as a future task.

CONCLUSION

The high-temperature single-atom catalyst Rh_1O_5/TiO_2 was prepared by substituting the Ti atoms of the TiO_2 surface lattice with Rh atoms. The singly dispersed Rh_1O_5 clusters exhibit extraordinary catalytic performance of POM at 650 °C including high activity, 98% selectivity for producing CO and 97% for H_2, long durability of 240 h, and high reusability over at least 20 cycles of catalysis. The single-atom site of this catalyst exhibits a turnover frequency of 2300 H_2 molecules per Rh_1 atom per minute at 650 °C under a kinetics-controlled regime. This extraordinary catalytic performance remains with no decay at 650 °C for at least 240 h. Computational studies suggest that (1) the activation energy of the rate-determining step, dehydrogenation of CH_3 to CH_2, is greatly decreased, while CH_3 and H bind to Rh_1 and O of the Rh_1O_5 cluster of this catalyst, respectively, and (2) the long catalytic durability of Rh_1/TiO_2 at 650 °C results from the unique coordination environment in which the Rh_1 atom on TiO_2 is in a nearly full coordination shell of oxygen atoms since Rh_1 coordinates with five oxygen atoms. Also benefiting from the nearly saturated coordination of Rh_1 on the TiO_2 surface, the adsorption energy of atomic carbon on Rh_1 is much lower than that on the Rh atom with an obviously unsaturated shell on the surface of a Rh NP. The single dispersion of Rh_1 atoms on Rh_1/TiO_2 and the low binding energy of atomic carbon on Rh_1 of the Rh_1/TiO_2 effectively prevent the Rh_1/TiO_2 from forming carbon layers at high temperature, where the formation of carbon layers in POM on currently reported catalysts remains a common phenomenon. This study suggests an avenue for single-atom catalysis in chemical transformations at high temperatures.

EXPERIMENTAL METHODS AND COMPUTATIONAL APPROACHES

Preparation of 0.037 wt % Rh/TiO_2 (Rh_1/TiO_2). A single atom catalyst, termed 0.037 wt % Rh/TiO_2 or Rh_1/TiO_2, was prepared with a modified deposition−precipitation method. Rhodium(III) nitrate hydrate, $Rh(NO_3)_3{\cdot}2H_2O$ (99.9%, Sigma-Aldrich), was used as the source of Rh cations for the preparation of the catalysts. A solution of Rh^{3+} with a concentration of 2.84×10^{-3} mol/L was made for the following use. TiO_2 nanopowder with primary particle size at 21 nm or so (Titania, ≥99.95%, Aeroxide P25, Sigma-Aldrich) were used as a TiO_2 support. The catalyst precursor of Rh_1/TiO_2 was prepared through a deposition−precipitation method modified for the preparation of single-atom catalyst Rh_1/TiO_2. In a typical experiment, 500 mg of TiO_2 was mixed with 50 mL of deionized water through a vigorous stirring to form a white suspension. A 3.0 mL $Rh(NO_3)_3{\cdot}2H_2O$ aqueous solution (2.84×10^{-3} mol/L) was introduced to the TiO_2 suspension through a precise injection with a syringe pump while the solution was vigorously stirred. The nominal loading is 0.20 wt %. The new suspension was continuously stirred for 2 h more to allow sufficient spontaneous adsorption of metal ions. The pH value of the mixture was carefully adjusted to 9.5 by gradually introducing an ammonium hydroxide solution, followed by vigorous stirring for another 6 h in order to reach a steady equilibrium in solution. Then, the prepared solution was centrifuged and then dried at 60 °C overnight with a following calcination in muffle furnace at 650 °C in air for 4 h. The measured loading of Rh with ICP-AES is only 0.037 wt %. Thus, either 0.037 wt % Rh/TiO_2 or Rh_1/TiO_2 was used in the text for referring to this catalyst.

As described above, 0.037 wt % Rh/TiO_2 was prepared through deposition−precipitation modified for this work. Based on the mechanism of the deposition−precipitation method, only a portion of cations were precipitated by OH^-. The portion of Rh^{3+} cations that can be precipitated on TiO_2 depends on the pH of the solution. A higher pH allows a larger portion of Rh^{3+} cations to be precipitated. To ensure the formation of singly dispersed Rh_1 on TiO_2 upon annealing at 650 °C in air instead of formation of Rh_2O_3 nanoparticles, the pH of the aqueous solution containing TiO_2 was controlled at 9.5. Based on ICP-AES measurements, the actual loading of Rh is 0.037 wt % Rh. Thus, only about 18.5% of the Rh^{3+} cations dissolved in water were precipitated. The rest of the Rh^{3+} cations remained in solution and then were washed out upon centrifugation to separate the TiO_2 with precipitated Rh^{3+} in the form of $Rh(OH)_3$ from the aqueous solution that contained the rest of the Rh^{3+}. Certainly, the Rh^{3+} in the aqueous solution can be readily reused by precipitation at high pH to form $Rh(OH)_3$; a following calcination in air makes Rh_2O_3. A reduction of Rh_2O_3 in H_2 forms Rh metal nanoparticles. Thus, the preparation of Rh_1/TiO_2 does not waste the precursor of Rh^{3+}.

Preparation of 6.3 wt % Rh/TiO_2 ($RhNP/TiO_2$). The 6.3 wt % Rh/TiO_2 catalyst was prepared via the impregnation method, which is distinctly different from the modified deposition−precipitation method. A 500 mg amount of the same type of TiO_2 powder as used for preparation of Rh_1/TiO_2 catalyst was introduced to 0.50 mL of an aqueous solution of $Rh(NO_3)_3{\cdot}2H_2O$ that contains 33.36 mg of Rh obtained from 85.18 mg of $Rh(NO_3)_3{\cdot}2H_2O$. The concentration of Rh would be 6.25 wt % if all Rh atoms could be transferred to the surface of TiO_2 based on the calculation $\frac{33.36\text{ mg Rh}}{33.36\text{ mg Rh} + 500\text{ mg TiO}_2} = 6.25$ wt %. The impregnated sample was dried in a 60 °C oven overnight and treated in flowing 5% H_2 in a tube furnace at 500 °C for 2 h and then at 650 °C for 4 h. Based on ICP measurements, the concentration of Rh loaded on TiO_2 is 6.3 wt %, which suggests most of the Rh atoms were transferred to TiO_2. Upon the above procedure, Rh nanoparticles were formed on TiO_2. Thus, either 6.3 wt % Rh/TiO_2 or Rh NP/TiO_2 was used in the text to refer to this catalyst, which is TiO_2 with loaded Rh NPs.

Compared to the preparation of single-atom catalysts described in the Experimental Methods and Computational Approaches section, the nanoparticle catalyst (6.3 wt % Rh/TiO_2 or termed Rh NP/TiO_2)

https://doi.org/10.1021/jacs.1c06432
J. Am. Chem. Soc. 2021, 143, 16566−16579

was prepared with the impregnation method instead of deposition−precipitation used for Rh_1/TiO_2. The impregnated sample was dried in a 60 °C oven in air overnight. Then, the dry catalyst precursor was treated in 5% H_2 at 500 and 650 °C instead of calcination in air at 650 °C. In the preparation of Rh_1/TiO_2, the pH of the aqueous solution containing TiO_2 and Rh^{3+} cations was carefully controlled at pH = 9.5. However, in the preparation of Rh NP/TiO_2, the solution containing a $Rh(NO_3)_3$ solution and TiO_2 is at about 7.0. In the precipitation for preparation of Rh_1/TiO_2, only about 20% Rh^{3+} cations were precipitated; however, in the preparation of Rh NP/TiO_2, all Rh^{3+} cations in solution were transferred to the surface of TiO_2. Thus, the preparations of the single-atom catalyst (Rh_1/TiO_2) and nanoparticle catalyst (Rh NP/TiO_2) were distinctly different.

DFT Calculations. The density functional theory (DFT) calculations were performed with the Vienna ab initio Simulation Package (VASP).[62] The on-site Coulomb interaction was included with the DFT+U method by Dudarev et al.[63] in VASP using a Hubbard parameter U = 3 eV for the Ti atom, from the previous literature for TiO_2.[64] The Perdew−Burke−Ernzerhof[65] functional form of the generalized-gradient approximation was used to describe electron exchange and correlation. In terms of the unit cell, we used a 1 × 3 supercell of the stable (101) surface facet of bulk anatase TiO_2. Regarding the distance between Rh atoms, the Rh atoms are separated by ∼10 Å along each axis of the cell. Regarding the Hubbard U correction, the Hubbard correction was applied for Ti d orbitals of the model. As there have yet to be any studies investigating the optimal U value for Rh in TiO_2, we opted to not include a correction for Rh, and we do not anticipate this will change the conclusions for the DFT calculations.

All calculations were performed with spin polarization. The projector-augmented wave method was used to describe the electron−core interaction with a kinetic energy cutoff of 450 eV. The Brillouin zone was sampled with the Monkhorst−Pack scheme of a 3 × 2 × 1 k-point mesh. Transition states (TSs) were found with the nudged elastic band (NEB) method using a force convergence criterion of 0.05 eV/Å. To calculate the occupancies of the molecular bonds of methane, the periodic NBO analysis implemented by Schmidt et al. was used.[66]

■ ASSOCIATED CONTENT

Supporting Information

The Supporting Information is available free of charge at https://pubs.acs.org/doi/10.1021/jacs.1c06432.

Size and morphology of 6.3 wt % Rh/TiO_2; chemisorption of CO on 0.037 wt % Rh/TiO_2 and 6.3 wt % Rh/TiO_2; evaluation of catalytic performances of bare TiO_2, 0.037 wt % Rh/TiO_2, and 6.3 wt % Rh/TiO_2; measurement of reaction rate under a kinetics-controlled regime; ex situ, in situ, and operando characterizations; calculations of the amount of Rh (in mol) *exposed to the surface* of 50 mg of 0.037 wt % Rh/TiO_2 and 50 mg of 6.3 wt % Rh/TiO_2; calculations of turnover rates of 0.037 wt % Rh/TiO_2 (Rh_1/TiO_2) and 6.3 wt % Rh/TiO_2 (Rh NP/TiO_2); note on the difference in coordination environment of Rh atoms in 0.037 wt % Rh/TiO_2 (Rh_1/TiO_2) and 6.3 wt % Rh/TiO_2 (Rh NP/TiO_2); note on AP-XPS studies; additional DFT structures and energetics (PDF)

■ AUTHOR INFORMATION

Corresponding Authors

De-en Jiang − *Department of Chemistry, University of California, Riverside, California 92521, United States*; Email: djiang@ucr.edu

Franklin Feng Tao − *Department of Chemical and Petroleum Engineering, University of Kansas, Lawrence, Kansas 66049, United States*; Email: franklin.tao.2017@gmail.com

Authors

Yu Tang − *Department of Chemical and Petroleum Engineering, University of Kansas, Lawrence, Kansas 66049, United States*

Victor Fung − *Department of Chemistry, University of California, Riverside, California 92521, United States;* Present Address: Center for Nanophase Materials Sciences, Oak Ridge National Laboratory, Oak Ridge, Tennessee 37831, United States

Xiaoyan Zhang − *Department of Chemical and Petroleum Engineering, University of Kansas, Lawrence, Kansas 66049, United States*

Yuting Li − *Department of Chemical and Petroleum Engineering, University of Kansas, Lawrence, Kansas 66049, United States;* orcid.org/0000-0003-2236-6612

Luan Nguyen − *Department of Chemical and Petroleum Engineering, University of Kansas, Lawrence, Kansas 66049, United States*

Tomohiro Sakata − *Innovation Research Center for Fuel Cells and Graduate School of Informatics and Engineering, The University of Electro-Communications, Chofu, Tokyo 182-8585, Japan*

Kotaro Higashi − *Innovation Research Center for Fuel Cells and Graduate School of Informatics and Engineering, The University of Electro-Communications, Chofu, Tokyo 182-8585, Japan*

Complete contact information is available at: https://pubs.acs.org/10.1021/jacs.1c06432

Author Contributions

¶Y.T., V.F., X.Z., and Y.L. equally contributed to this work.

Notes

The authors declare no competing financial interest.

■ ACKNOWLEDGMENTS

The experimental part was supported by the NSF Career Award NSF-CHE-1462121 and Chemical Sciences, Geosciences and Biosciences Division, Office of Basic Energy Sciences, Office of Science, U.S. Department of Energy, under Grant No. DE-SC0014561. The DFT computation was supported by the Grant No. DE-SC0014561 before September 1, 2019; afterwards, it was supported by Eugene P. Wigner Fellowship at ORNL (V.F.) and NSF CBET-1924545 (D.J.). The offer of beam time from the Innovation Research Center for Fuel Cells at The University of Electro-Communications and the assistance in data collection at Japan were highly appreciated. F.T. deeply thanks Dr. M. Chi at ORNL for TEM studies of a part of the Rh_1/TiO_2 samples of this work and Dr. W. Huang at Iowa State Univ. for assisting in DRIFT studies of some of the Rh_1/TiO_2 samples. F.T. appreciates collaborators at FZU for offering a significant amount of machine time for free access to their high-resolution TEM and other characterization instruments for extensive studies of samples before and after catalysis. Without the access to these characterization instruments of collaborators at FZU, it would have been impossible to finish this work at all. This work does not contain any classified information. All experimental data and details of this work were/are published as the DOE and NSF projects

acknowledged here were funded by the Chemistry Division of NSF and Office of Science of the DOE with the goal of pursuing a publishable fundamental understanding of the science of catalytic chemistry instead of any technique or know-how with commercial value. None of the authors of this work thinks any part of this work could have any potential commercial value. None of these authors of this work thinks any part of this work could be combined or mingled with other work to generate classified information or commercial value.

REFERENCES

(1) Pena, M. A.; Gomez, J. P.; Fierro, J. L. G. New catalytic routes for syngas and hydrogen production. *Appl. Catal., A* **1996**, *144*, 7−57.
(2) York, A. P. E.; Xiao, T. C.; Green, M. L. H. Brief overview of the partial oxidation of methane to synthesis gas. *Top. Catal.* **2003**, *22*, 345−358.
(3) Tsang, S. C.; Claridge, J. B.; Green, M. L. H. Recent advances in the conversion of methane to synthesis gas. *Catal. Today* **1995**, *23*, 3−15.
(4) Vernon, P. D. F.; Green, M. L. H.; Cheetham, A. K.; Ashcroft, A. T. Partial oxidation of methane to synthesis gas. *Catal. Lett.* **1990**, *6*, 181−186.
(5) Byrne, P. J., Jr.; Gohr, E. J.; Elizabeth, N. J.; Haslam, R. T. Recent Progress in Hydrogenation of Petroleum. *Ind. Eng. Chem.* **1932**, *24*, 1129−1135.
(6) Nahar, G.; Dupont, V. Hydrogen production from simple alkanes and oxygenated hydrocarbons over ceria-zirconia supported catalysts: Review. *Renewable Sustainable Energy Rev.* **2014**, *32*, 777−796.
(7) Amin, A. M.; Croiset, E.; Epling, W. Review of methane catalytic cracking for hydrogen production. *Int. J. Hydrogen Energy* **2011**, *36*, 2904−2935.
(8) Enger, B. C.; Lodeng, R.; Holmen, A. A review of catalytic partial oxidation of methane to synthesis gas with emphasis on reaction mechanisms over transition metal catalysts. *Appl. Catal., A* **2008**, *346*, 1−27.
(9) Liander, H. The utilisation of natural gases for the ammonia process. *Trans. Faraday Soc.* **1929**, *25*, 462−472.
(10) Prettre, M.; Eichner, C.; Perrin, M. The catalytic oxidation of methane to carbon monoxide and hydrogen. *Trans. Faraday Soc.* **1946**, *42*, 335b−339.
(11) Dissanayake, D.; Rosynek, M. P.; Kharas, K. C. C.; Lunsford, J. H. Partial Oxidation of Methane to Carbon-Monoxide and Hydrogen over a Ni/Al_2O_3 Catalyst. *J. Catal.* **1991**, *132*, 117−127.
(12) Choudhary, V. R.; Mamman, A. S.; Sansare, S. D. Selective Oxidation of Methane to CO and H_2 over Ni/MGO at Low-Temperatures. *Angew. Chem., Int. Ed. Engl.* **1992**, *31*, 1189−1190.
(13) Choudhary, V. R.; Rajput, A. M.; Rane, V. H. Low-Temperature Catalytic Selective Partial Oxidation of Methane to CO and H_2 over Ni/YB_2O_3. *J. Phys. Chem.* **1992**, *96*, 8686−8688.
(14) Choudhary, V. R.; Rajput, A. M.; Prabhakar, B. Nonequilibrium Oxidative Conversion of Methane to CO and H_2 with High Selectivity and Productivity over Ni/Al_2O_3 at Low-Temperatures. *J. Catal.* **1993**, *139*, 326−328.
(15) Ruckenstein, E.; Hul, Y. H. Methane partial oxidation over NiO MgO solid solution catalysts. *Appl. Catal., A* **1999**, *183*, 85−92.
(16) Hu, Y. H.; Ruckenstein, E. Catalyst temperature oscillations during partial oxidation of methane. *Ind. Eng. Chem. Res.* **1998**, *37*, 2333−2335.
(17) Santos, A.; et al. Oxidation of methane to synthesis gas in a fluidized bed reactor using MgO-based catalysts. *J. Catal.* **1996**, *158*, 83−91.
(18) Lu, Y.; Liu, Y.; Shen, S. K. Design of stable Ni catalysts for partial oxidation of methane to synthesis gas. *J. Catal.* **1998**, *177*, 386−388.
(19) Liu, S.; et al. Sustainable Ni catalyst for partial oxidation of CH_4 to syngas at high temperature. *Stud. Surf. Sci. Catal.* **2000**, *130*, 3567−3572.
(20) Choudhary, V. R.; Uphade, B. S.; Mamman, A. S. Partial oxidation of methane to syngas with or without simultaneous CO(2) and steam reforming reactions over NiAlPO4. *Microporous Mesoporous Mater.* **1998**, *23*, 61−66.
(21) Hayakawa, T.; et al. A sustainable catalyst for the partial oxidation of methane to syngas: $Ni/Ca_{1-x}Sr_xTiO_3$, prepared in situ from perovskite precursors. *Angew. Chem., Int. Ed. Engl.* **1996**, *35*, 192−195.
(22) Basile, F.; et al. Ni/Mg/Al anionic clay derived catalysts for the catalytic partial oxidation of methane - Residence time dependence of the reactivity features. *J. Catal.* **1998**, *173*, 247−256.
(23) Peters, K.; Rudolf, M.; Voetter, H. On the reaction pathway of methane reforming (germ.). *Brennstoff-Chemie* **1955**, *36*, 257.
(24) Ashcroft, A. T.; et al. Selective Oxidation of Methane to Synthesis Gas-Using Transition-Metal Catalysts. *Nature* **1990**, *344*, 319−321.
(25) Choudhary, V. R.; Prabhakar, B.; Rajput, A. M.; Mamman, A. S. Oxidative conversion of methane to CO and H_2 over Pt or Pd containing alkaline and rare earth oxide catalysts. *Fuel* **1998**, *77*, 1477−1481.
(26) York, A. P. E.; Claridge, J. B.; Brungs, A. J.; Tsang, S. C.; Green, M. L. H. Molybdenum and tungsten carbides as catalysts for the conversion of methane to synthesis gas using stoichiometric feedstocks. *Chem. Commun.* **1997**, 39−40.
(27) York, A.; et al. In *Studies on Surface Science Catalysis*; Elsevier, 1997; Vol. *110*, pp 711−720.
(28) Claridge, J. B.; et al. New catalysts for the conversion of methane to synthesis gas: Molybdenum and tungsten carbide. *J. Catal.* **1998**, *180*, 85−100.
(29) Qiao, B.; et al. Single-atom catalysis of CO oxidation using Pt_1/FeO_x. *Nat. Chem.* **2011**, *3*, 634−641.
(30) Yang, X.-F.; et al. Single-Atom Catalysts: A New Frontier in Heterogeneous Catalysis. *Acc. Chem. Res.* **2013**, *46*, 1740−1748.
(31) Liang, S.; Hao, C.; Shi, Y. The Power of Single-Atom Catalysis. *ChemCatChem* **2015**, *7*, 2559−2567.
(32) Lang, R.; et al. Hydroformylation of Olefins by a Rhodium Single-Atom Catalyst with Activity Comparable to $RhCl(PPh_3)_3$. *Angew. Chem., Int. Ed.* **2016**, *55*, 16054−16058.
(33) Sun, Q.; et al. Zeolite-Encaged Single-Atom Rhodium Catalysts: Highly-Efficient Hydrogen Generation and Shape-Selective Tandem Hydrogenation of Nitroarenes. *Angew. Chem., Int. Ed.* **2019**, *58*, 18570−18576.
(34) Tang, Y.; et al. Rh single atoms on TiO_2 dynamically respond to reaction conditions by adapting their site. *Nat. Commun.* **2019**, *10*, 4488.
(35) Wang, L.; et al. Atomic-level insights in optimizing reaction paths for hydroformylation reaction over Rh/CoO single-atom catalyst. *Nat. Commun.* **2016**, *7*, 14036.
(36) Guan, H.; et al. Enhanced performance of Rh_1/TiO_2 catalyst without methanation in water-gas shift reaction. *AIChE J.* **2017**, *63*, 2081−2088.
(37) Han, B.; et al. A highly active Rh_1/CeO_2 single-atom catalyst for low-temperature CO oxidation. *Chem. Commun.* **2020**, *56*, 4870−4873.
(38) Ma, X.-L.; Liu, J.-C.; Xiao, H.; Li, J. Surface Single-Cluster Catalyst for N_2-to-NH_3 Thermal Conversion. *J. Am. Chem. Soc.* **2018**, *140*, 46−49.
(39) Matsubu, J. C.; et al. Adsorbate-mediated strong metal-support interactions in oxide-supported Rh catalysts. *Nat. Chem.* **2017**, *9*, 120−127.
(40) Tang, Y.; et al. Single rhodium atoms anchored in micropores for efficient transformation of methane under mild conditions. *Nat. Commun.* **2018**, *9*, 1231.
(41) Shan, J.; Li, M.; Allard, L. F.; Lee, S.; Flytzani-Stephanopoulos, M. Mild oxidation of methane to methanol or acetic acid on supported isolated rhodium catalysts. *Nature* **2017**, *551*, 605.
(42) Nguyen, L.; et al. Reduction of Nitric Oxide with Hydrogen on Catalysts of Singly Dispersed Bimetallic Sites Pt_1Co_m and Pd_1Co_n. *ACS Catal.* **2016**, *6*, 840−850.

https://doi.org/10.1021/jacs.1c06432
J. Am. Chem. Soc. 2021, 143, 16566−16579

(43) Leclerc, C. A.; Redenius, J. M.; Schmidt, L. D. Fast lightoff of millisecond reactors. *Catal. Lett.* **2002**, *79*, 39−44.
(44) Schmidt, L. D. In *Studies in Surface Science and Catalysis*; Elsevier, 2000; Vol. *130*, pp 61−81.
(45) An, K.; Somorjai, G. A. Size and Shape Control of Metal Nanoparticles for Reaction Selectivity in Catalysis. *ChemCatChem* **2012**, *4*, 1512−1524.
(46) Borodko, Y.; Ercius, P.; Pushkarev, V.; Thompson, C.; Somorjai, G. From Single Pt Atoms to Pt Nanocrystals: Photoreduction of Pt^{2+} Inside of a PAMAM Dendrimer. *J. Phys. Chem. Lett.* **2012**, *3*, 236−241.
(47) Borodko, Y.; et al. From Single Atoms to Nanocrystals: Photoreduction of $[PtCl_6]^{2-}$ in Aqueous and Tetrahydrofuran Solutions of PVP. *J. Phys. Chem. C* **2013**, *117*, 26667−26674.
(48) Glover, E. N. K.; Ellington, S. G.; Sankar, G.; Palgrave, R. G. The nature and effects of rhodium and antimony dopants on the electronic structure of TiO_2: towards design of Z-scheme photocatalysts. *J. Mater. Chem. A* **2016**, *4*, 6946−6954.
(49) Grunwaldt, J. D.; Basini, L.; Clausen, B. S. In situ EXAFS study of Rh/Al_2O_3 catalysts for catalytic partial oxidation of methane. *J. Catal.* **2001**, *200*, 321−329.
(50) Dohmae, K.; Seno, Y. Local structure change of Rh on alumina after treatments in high-temperature oxidizing and reducing environments. *Surf. Interface Anal.* **2005**, *37*, 115−119.
(51) Krenn, G.; Bako, I.; Schennach, R. CO adsorption and CO and O coadsorption on Rh(111) studied by reflection absorption infrared spectroscopy and density functional theory. *J. Chem. Phys.* **2006**, *124*, 124.
(52) Bouchet, R.; Weibel, A.; Knauth, P.; Mountjoy, G.; Chadwick, A. V. EXAFS study of dopant segregation (Zn, Nb) in nanocrystalline anatase (TiO_2). *Chem. Mater.* **2003**, *15*, 4996−5002.
(53) Wu, Q.; Zheng, Q.; van de Krol, R. Creating Oxygen Vacancies as a Novel Strategy To Form Tetrahedrally Coordinated Ti^{4+} in Fe/TiO_2 Nanoparticles. *J. Phys. Chem. C* **2012**, *116*, 7219−7226.
(54) Nguyen, L.; Tao, F. F.; Tang, Y.; Doug, J.; Bao, X.-J. Understanding Catalyst Surfaces during Catalysis through Near Ambient Pressure X-ray Photoelectron Spectroscopy. *Chem. Rev.* **2019**, *119*, 6822−6905.
(55) Hall, C.; Perutz, R. N. Transition metal alkane complexes. *Chem. Rev.* **1996**, *96*, 3125−3146.
(56) Weaver, J. F.; Hakanoglu, C.; Antony, A.; Asthagiri, A. Alkane activation on crystalline metal oxide surfaces. *Chem. Soc. Rev.* **2014**, *43*, 7536−7547.
(57) Liang, Z.; Li, T.; Kim, M.; Asthagiri, A.; Weaver, J. F. Low-temperature activation of methane on the $IrO_2(110)$ surface. *Science* **2017**, *356*, 298−301.
(58) Saillard, J. Y.; Hoffmann, R. C-H AND H-H Activation in Transition-Metal Complexes and on Surfaces. *J. Am. Chem. Soc.* **1984**, *106*, 2006−2026.
(59) Liu, J.; et al. Tuning Catalytic Selectivity of Oxidative Catalysis through Deposition of Nonmetallic Atoms in Surface Lattice of Metal Oxide. *ACS Catal.* **2016**, *6*, 4218−4228.
(60) Siemer, N.; et al. Atomic-Scale Explanation of O_2 Activation at the Au-TiO_2 Interface. *J. Am. Chem. Soc.* **2018**, *140*, 18082−18092.
(61) Brugnoli, L.; Pedone, A.; Menziani, M. C.; Adamo, C.; Labat, F. O_2 Activation over Ag-Decorated $CeO_2(111)$ and $TiO_2(110)$ Surfaces: A Theoretical Comparative Investigation. *J. Phys. Chem. C* **2020**, *124*, 25917−25930.
(62) Kresse, G.; Furthmuller, J. Efficient iterative schemes for ab initio total-energy calculations using a plane-wave basis set. *Phys. Rev. B: Condens. Matter Mater. Phys.* **1996**, *54* (16), 11169−11186.
(63) Dudarev, S. L.; Botton, G. A.; Savrasov, S. Y.; Humphreys, C. J.; Sutton, A. P. Electron-energy-loss spectra and the structural stability of nickel oxide: An LSDA+U study. *Phys. Rev. B: Condens. Matter Mater. Phys.* **1998**, *57* (3), 1505−1509.
(64) Hu, Z.; Metiu, H. Choice of U for DFT plus U Calculations for Titanium Oxides. *J. Phys. Chem. C* **2011**, *115* (13), 5841−5845.
(65) Perdew, J. P.; Burke, K.; Ernzerhof, M. Generalized Gradient Approximation Made Simple. *Phys. Rev. Lett.* **1996**, *77* (18), 3865−3868.
(66) Dunnington, B. D.; Schmidt, J. R. Generalization of Natural Bond Orbital Analysis to Periodic Systems: Applications to Solids and Surfaces via Plane-Wave Density Functional Theory. *J. Chem. Theory Comput.* **2012**, *8* (6), 1902−1911.

https://doi.org/10.1021/jacs.1c06432
J. Am. Chem. Soc. 2021, 143, 16566−16579